Magnesium Nanoparticle Plasmonics

John S. Biggins,[1] Sadegh Yazdi,[2] Emilie Ringe[2,3,4,5]

1. Department of Engineering, University of Cambridge, Trumpington Street, Cambridge CB2 1PZ, U.K.

2. Department of Material Science and Nanoengineering, 6100 Main Street, Houston, Texas 77005, United States

3. Department of Chemistry, Rice University, 6100 Main Street, Houston, Texas 77005, United States

4. Department of Materials Science and Metallurgy, University of Cambridge, 27 Charles Babbage Road, Cambridge CB3 0FS, U.K.

5. Department of Earth Sciences, University of Cambridge, Downing Street, Cambridge CB2 3EQ, U.K.

Corresponding author email: er407@cam.ac.uk

ABSTRACT

Nanoparticles of some metals (Cu/Ag/Au) sustain oscillations of their electron cloud called localized surface plasmon resonances (LSPRs). These resonances can occur at optical frequencies and be driven by light, generating enhanced electric fields and spectacular photon scattering. However, current plasmonic metals are rare, expensive, and have a limited resonant frequency range. Recently, much attention has been focused on earth-abundant Al, but Al nanoparticles cannot resonate in the IR. The earth-abundant Mg nanoparticles reported here surmount this limitation. A colloidal synthesis forms hexagonal nanoplates, reflecting Mg's simple hexagonal lattice. The NPs form a thin self-limiting oxide layer that renders them stable suspended in 2-propanol solution for months and dry in air for at least two week. They sustain LSPRs observable in the far-field by optical scattering spectroscopy. Electron energy loss spectroscopy experiments and simulations reveal multiple size-dependent resonances with energies across the UV, visible, and IR. The symmetry of the modes and their interaction with the underlying substrate are studied using numerical methods. Colloidally synthesized Mg thus offers a route to inexpensive, stable nanoparticles with novel shapes and resonances spanning the entire UV-vis-IR spectrum, making them a flexible addition to the nanoplasmonics toolbox.

KEYWORDS

Metal nanoparticles, Localized surface plasmon resonance, Magnesium, Plasmonics, Electron-energy loss spectroscopy

MAIN TEXT

Localized surface plasmon resonances (LSPRs) in Ag and Au NPs have been used since ancient times to impart brilliant colors to glass. Over the past decades, they have been intensively studied by scientists and engineers, who have unraveled their modes of oscillation and sought applications including cancer therapy,[1] enhanced spectroscopy,[2,3] sensing,[4,5] and photocatalysis.[6,7] However, the stable of plasmonic metals has only very recently expanded beyond Au and Ag, to encompass first Cu[8] then, most recently, Al, for which an increasingly large amount of work has been published.[9-18] Several other elements and compounds, including Earth-abundant elements, have been predicted or observed to sustain LSPRs,[9,19-32] offering opportunities to surmount the cost challenges associated with the rare metals Ag and Au, and the limited frequency range of resonances in all known plasmonic metals.[10,11,19,20,31,33,34] Left of Al in the periodic table is Mg, another metal predicted to be a good plasmonic material,[9,19] with resonances potentially spanning the UV-vis-NIR wavelength ranges. The existence of these plasmonic effects in Mg have very recently been confirmed by optical studies of fabricated Mg nanostructures: Jeong *et al*. used glancing angle deposition to produce Ti-doped Mg helices exhibiting chiral photoresponse,[35] Sterl *et al*. utilized hole-mask lithography to produce Mg nanodisks with intense visible light absorption,[36] Wang *et al*. described how ion beam milled Mg aperture films can manipulate fluorescence radiation rates more strongly than Al films,[37] and Duan *et al.* reported the use of plasmonic Mg square arrays as dynamic pixels based on reversible Mg hydrogenation.[38] However, top-down fabricated Mg structures have many practical drawbacks: they are expensive and slow to produce and often have poor crystallinity potentially impacting LSPR quality and stability. Furthermore, optical studies, inhibited by the diffraction limit, struggle to unravel the underlying sub-wavelength details of plasmon behavior

that control nanoscale interactions. Taking our cue from the important body of work on Au, Ag, and Al, here we combine optical spectroscopy, electron spectroscopy and numerical simulations to fully characterize the plasmon modes of colloidally synthesized[39] discrete Mg nanocrystals. Excitingly, and unlike Au, Ag, and Cu which all have upper energy bounds to resonances in the blue or UV owing to bulk plasmons and interband transitions, and unlike Al which has lower energy bounds in the near-IR owing to interband transitions,[11,33,40,41] Mg's LSPR modes span the entire UV-visible-IR frequency range, here from 3.8 to 1.3 eV.

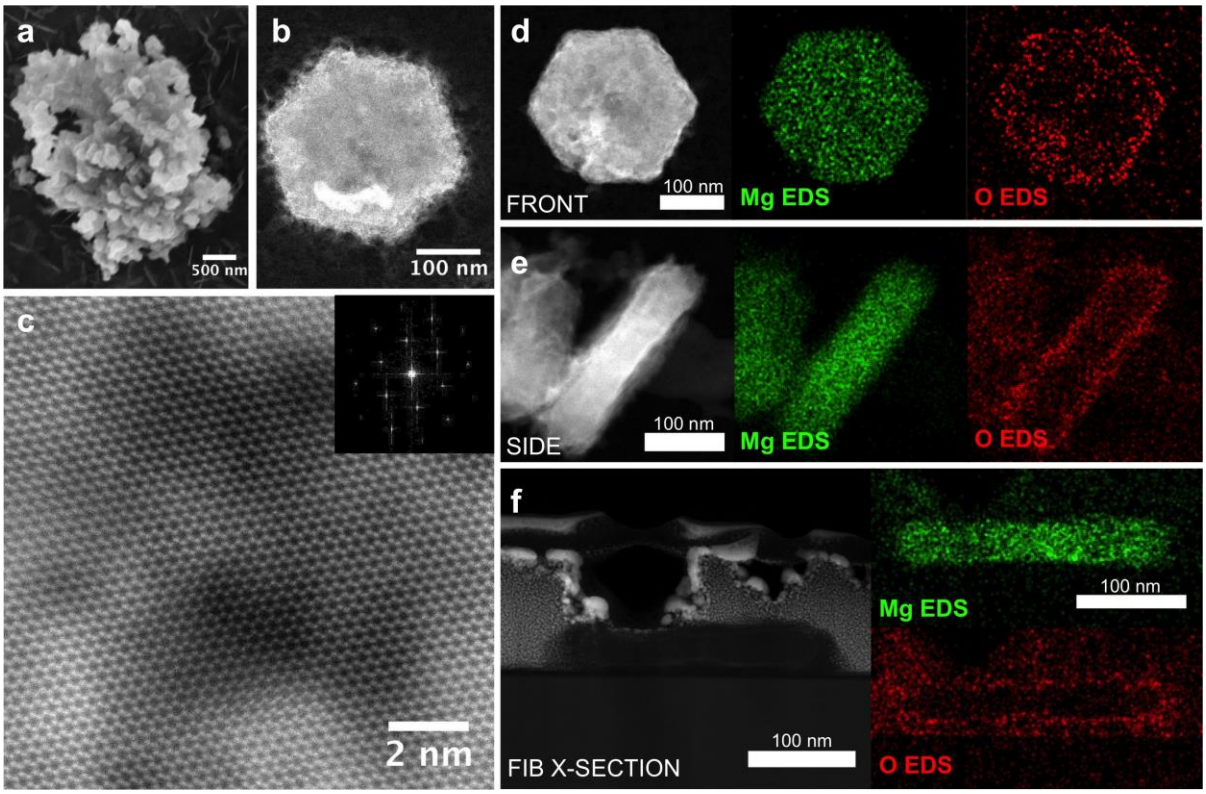

Figure 1. Morphology, crystallography, and composition of hexagonal Mg nanoplates. a) SEM image of a large aggregate, b) HAADF-STEM image of a single NP, c) HAADF-STEM atomic resolution image (and associated FFT) of the center of the NP in b, showing the simple hexagonal lattice of Mg along the [0001] axis. HAADF-STEM images and associated Mg and O

STEM-EDS maps of a nanoplate (d) perpendicular and (e) parallel to the electron beam. f) HAADF-STEM image of a FIB-cut section of a hexagonal NP viewed edge-on, and Mg and O STEM-EDS maps showing the ~5 nm Mg oxide at the NP surface, note that the thin SiO_2 native oxide on the Si substrate can also be seen below the NP. Additional images, composition linescans, and composition characterization data reported in Figure S1-5.

The synthesis of colloidal Mg and MgO nanoparticles, which has previously been reported, can be performed by reaction of a Mg organometallic precursor such as di-n-butyl magnesium[39] or bis(cyclopentadienyl)magnesium.[42,43] Here, a mixture of Li and naphthalene was sonicated for an hour, yielding a deep dark green solution of lithium naphtalide, then used in a 16:7 excess to reduce di-n-butyl magnesium in anhydrous tetrahydrofuran[39] under an Ar atmosphere. In this process, as discussed in ref.[39], the butyl groups of di-n-butyl magnesium are transferred to Li, resulting in Mg, naphthalene, and BuLi. The Mg NPs were then centrifuged and redispersed in 2-propanol. The main reaction product is single-crystalline hexagonal Mg nanoplates (Figure 1). This shape derives from the simple hexagonal lattice (hcp) of metallic Mg (Figure 1c), and exposes low index facets belonging to the {0001} (top and bottom) and {1-100} (six sides) families of planes. Scanning electron microscopy (SEM) and scanning transmission electron microscopy (STEM) analysis of face-on particles reveals the nanoplates have tip-to-tip diameters (size) ranging from 100 to 300 nm, consistent with light scattering results revealing a mean size of 166 nm with a standard deviation of 45 nm. Analysis of edge-on and focused ion beam cut NPs (Figure S4) reveals Mg thicknesses ranging from ~30 to 60 nm.

STEM-energy dispersive X-ray spectroscopy (STEM-EDS) and STEM-electron energy loss spectroscopy (STEM-EELS), and powder X-ray diffraction confirmed that the hexagonal nanoplates are indeed mainly composed of metallic Mg (Figure 1 and S2-3). STEM-EDS maps

reveal a thin layer of Mg oxide homogeneously surrounding the NPs. Mapping of a NP roughly perpendicular to the c axis (Figure 1e) reveals the surface localization of oxygen. This is further supported by STEM-EDS maps from a thin NP cross-section prepared by FIB milling (Figure 1f). An oxide layer thickness of 6-7 nm is observed in the FIB-cut samples, a reliable measurement owing to the creation of a NP "slice" free from edges and terminal facets along the beam direction. This thickness is similar to the native oxide layer observed on Al NPs and comparable to the few nm observed in bulk Mg.[10,44] STEM-EELS and STEM-EDS measurements of entire NPs (Figure 1 and Figures S3-5) provide thickness values of 20 to 30 nm, an upper bound considering potential NP tilt with respect to the beam and the contribution of NP edges.[44] This oxide, likely formed during synthesis workup, is self-limiting and stabilizes the NPs for months, as will be discussed later.

The NP solution is grey-ish green with a broad extinction spectrum (Figure 2), although a peak is evident around 700 nm, offering the first suggestion of plasmonic behavior. The broadness of the extinction signature is likely caused by size heterogeneity and particle aggregation. These difficulties can be overcome by studying NPs one at a time. Far-field optical scattering spectra of single NPs drop cast on glass and sealed in a thin 2-propanol liquid cell were recorded in the ~450-850 nm range with a dark field geometry.[45,46] Strong scattering was observed from both immobilized and the occasional floating NPs (Figure 2b, Figure S6, and Supporting Video 1), with characteristic spectra showing a dominant peak between 600 and ~800 nm, and sometimes a second lower wavelength peak within the 450-850 nm optical window.

The plasmonic origin of these peaks is confirmed by numerical calculations of light scattering by 30nm thick Mg hexagonal NPs, performed in the discrete dipole approximation with DDSCAT.[47,48] Figure 2c shows the calculated scattering spectrum for three different diameters of

Mg hexagonal nanoplates (162, 218 and 272 nm tip-to-tip) spanning the experimental size distribution. These calculations precisely reproduced the conditions in the single particle dark-field scattering experiments, including a 5nm thick coating of MgO around the NPs, a glass substrate beneath them, an ambient media of 2-propanol, and a light bean incident at 59° to the particle normal. Each spectrum shows four distinct peaks, corresponding to four plasmon resonances, which, from long to short wavelength, we call LSPRs 1-4. The peak locations for LSPRs 1 (700, 855 and 995 nm) and 2 (490, 575 and 665 nm) are strongly size dependent, a hallmark of localized surface plasmon phenomena. One or both of these peaks is seen in each experimental single particle spectrum, depending on particle size, as expected given the experimental optical window of 450-850 nm. These two peak locations also overlap, so in bulk extinction they merge into the dominant broad long-wavelength peak. In contrast, LSPRs 3 and 4 have non-overlapping peak positions that lie below the single particle scattering window, but generate the two small short-wavelength peaks in the bulk extinction spectrum. Overall, the optical experiments and simulations are in excellent agreement, and suggest that colloidally synthesized Mg NPs sustain at least four optically active LSPRs spanning from the UV to the IR.

To aid later interpretation of our results, we also calculated spectra with increasingly simplified geometries, reported in Figure S7. Changing the light to normal incidence eliminates the peaks for LSPRs 2 and 3. In contrast, additionally removing the substrate (thereby modeling a particle floating in 2-propanol, as is observed in bulk extinction) has only a marginal effect on peak location, justifying the application of our original spectra to the experimental extinction spectrum. Finally, removing the 2-propanol and the MgO layer from the calculations resulted in a substantial blue shift. Overall, these observations highlight the importance of correctly

measuring and modeling experimental conditions in order to obtain a reliable numerical/experimental agreement.

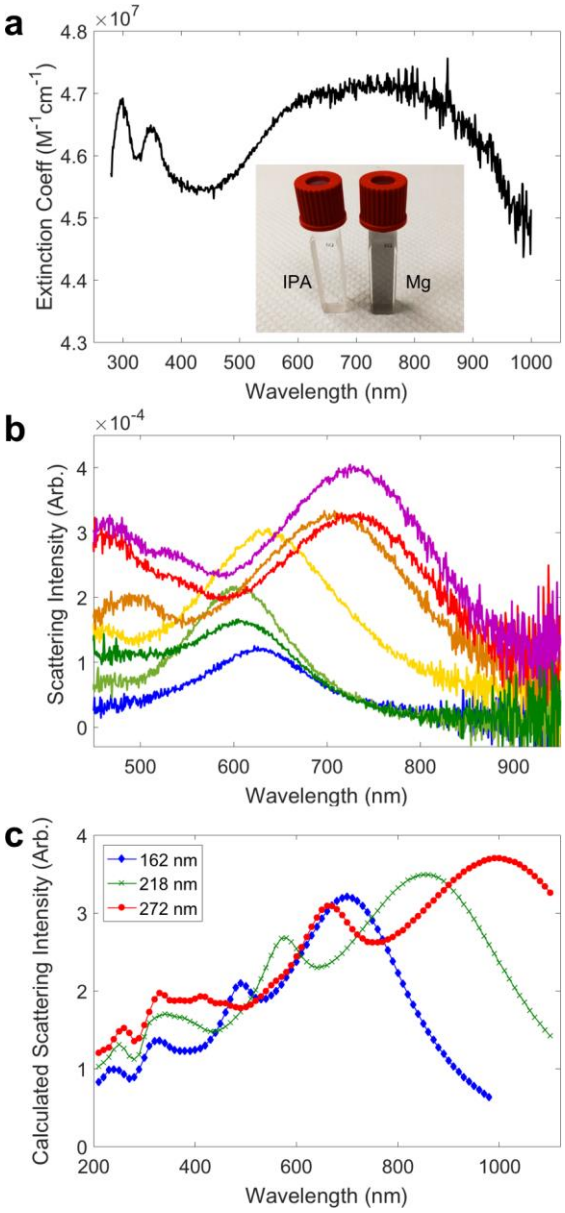

Figure 2. Optical properties of hexagonal Mg nanoplates. a) Extinction coefficient (per M of NPs) calculated from the UV-vis-NIR extinction spectrum and the light scattering-determined NP concentration (Figure S2), the inset shows a picture of the Mg NP solution and 2-propanol (IPA) for reference. b) Experimental dark-field scattering spectra for seven single NPs

immobilized on glass and submerged in 2-propanol, additional spectra reported in Figure S6. c) Numerical scattering spectra for three diameters of Mg NPs homogeneously coated with 5 nm MgO, on a glass substrate (refractive index RI = 1.5) submerged in 2-propanol (RI = 1.378), with the light bean incident at 59° to the particle normal. Additional numerical optical results in Figure S7-8.

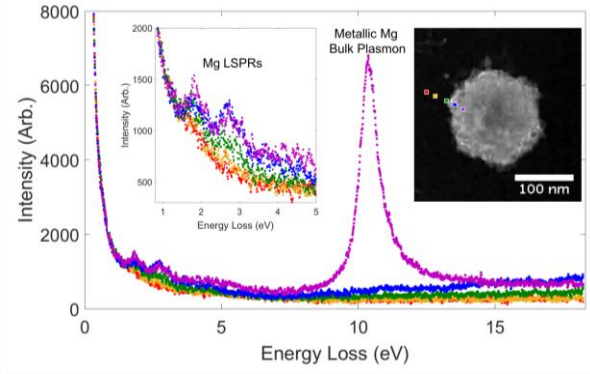

Figure 3. Spatial dependence of the electron energy loss spectroscopy (EELS) response of a Mg nanoplate on a Si_3N_4 substrate, showing the metallic Mg bulk plasmon at ~10.4 eV when the beam penetrates the core of the NP, and multiple LSPRs in the 1-5 eV range. Spectra in the main panel and the left inset are raw spectra binned 2 pixels *x* 2 pixels from the color-coded positions shown in the right inset. The size of the squares in the inset is exaggerated (2 *x* actual side length) for clarity. EELS spectra for eight additional NPs are reported in Figure S9.

To unravel the nature of these resonances, as well as their near-field properties, we conducted low-loss STEM-EELS studies[49-57] on 9 Mg NPs of sizes ranging from 162 to 273 nm. These experiments were performed on Mg nanoplates supported on a thin Si_3N_4 membrane in a monochromated, probe-corrected FEI Titan Themis[3] operated at 300 kV (Zero loss peak FWHM

~0.15 eV). Characteristic STEM-EELS spectra obtained for a 162 nm particle and spanning the UV-Vis-NIR range are shown in Figure 3. These spectra report the probability of an incident electron losing a given amount of energy in its path through the NP, due to LSPRs or other phenomena. In Figure 3, a large peak appears at ~10.4 eV when the beam passes through the NP, corresponding to the excitation of a bulk plasmon in metallic Mg,[43] confirming the presence of metallic Mg. A broader, weaker absorption in the 10-20 eV range and beyond is visible when the beam penetrates the thin surface oxide layer; this response corresponds to MgO.[43] Finally, the low loss region (inset of Figure 3) features several peaks when the beam is the surface of the NP; these peaks are attributed to LSPRs and, as expected, decrease in intensity with increasing distance from the NP.

In order to gain a spatial understanding of these modes, a full EELS spectrum was gathered at each ~2 nm pixel in a ~200 pixels × 200 pixels map (typical values) spanning the NP and its surroundings, creating a STEM-EELS spectrum image, or data cube. We then used Gaussian fitting to extract the mode spatial distributions and frequencies from each spectrum image. Briefly, we fit each (background-subtracted) spectrum image with four Gaussian spectral peaks, each associated with a spatial EELS intensity image. The positions, heights, and widths of the Gaussians selected by the fit reveal the spectral position, strength, and width of the resonances, while the associated intensity image encodes the spatial signature of each LSPR mode, as shown in Figure 4. The first (lowest energy) peak is associated with a diffuse ring of EEL intensity around the edge of the hexagonal plate, the second peak is associated with strong intensity at the corners and the third (highest energy) peak has intensity at the hexagon's edges and center. The fourth Gaussian fits the broad high energy tail, which probably corresponds to a large collection of high order modes.

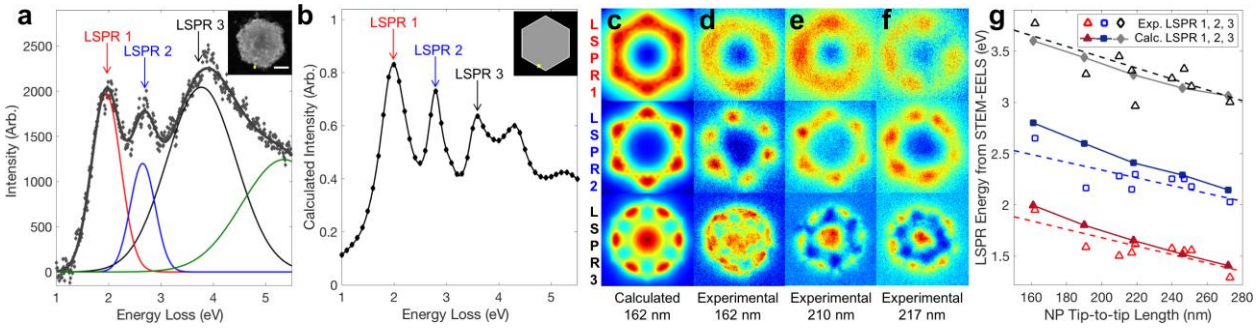

Figure 4. Near-field plasmonic behavior of Mg NPs. a) Experimental background-subtracted STEM-EELS spectrum (grey diamonds) and Gaussian fits for a 162 nm Mg nanoplate, binned from the 5 pixel x 5 pixel (12 nm x 12 nm) position shown in the inset, scalebar, 100 nm. b) Calculated EELS spectrum for a 162 nm Mg nanoplate coated with 5 nm MgO on a Si_3N_4 substrate at the position shown in the inset. c) Calculated and d-f) experimental STEM-EELS intensity distribution for Mg nanoplates. g) Experimental (open markers, dashed lines, N = 9) and calculated (filled markers, solid lines, N = 5) size dependence of the three lowest energy LSPRs. Numerical values for Gaussian fits and size dependences reported in Tables S1-2. EELS maps for eight additional NPs are reported in Figure S10.

Similar patterns were found for each mode in all the particles but the position of each peak, which relates to the resonant frequency of the underlying LSPR, shifted in a statistically significant fashion with NP size (Figure 4 and Tables S1-2) with larger particles having lower energy resonances. Such size scaling is expected from phase retardation effects in plasmonic nanostructures,[46,58] and is the hallmark of LSPRs. The slope of the LSPR energy vs size plot ranges from 3.8(standard deviation, 1.3) to -5.3(1.8) meV/nm, comparable to the 2.96(6) meV/nm obtained for a variety of Au NP shapes.[46] Together, Mg NP's three plasmon resonances

span the UV, visible and near-IR spectrum, from 3.8 to 1.3 eV (325 nm to 950 nm). The presence of multiple size-dependent modes was further confirmed by other spectral deconvolution and data cube analysis techniques (Figure S11-13). This holds significant promise for the applicability of Mg nanoparticles in plasmonics, where wavelength tunability is of critical importance.

To corroborate and extend our understanding of these plasmon modes, we performed numerical simulations of the interaction between Mg nanoplates and an electron beam using the e-DDA code,[54] which is based on the discrete dipole code DDSCAT.[47,48] A simulated EELS spectrum for a 162 nm wide, 30 nm thick Mg hexagonal plate covered homogeneously in 5 nm MgO and supported on 20 nm Si_3N_4 is shown in Figure 4b. The match to the experimental data is excellent, reproducing three main peaks at 2.0, 2.8, and 3.6 eV, compared to the experimental peaks at 1.91, 2.71 and 3.75 eV. Furthermore, simulated EELS images for the three peaks, which map the EELS intensity at each incident beam position and at a given energy loss, reproduce the experimental patterns: the lowest energy peak corresponds to a diffuse ring, the second, to a corner mode, and the third, to an edge mode with additional intensity in the center of the NP (Figure 4c-f); the symmetry of these modes does not change significantly with size. Calculations for NPs of different sizes predict a redshift of the peak with increasing size (Figure 4g, S14), in excellent agreement with the experiments. This experimental-numerical match, achieved without adjustable computational parameters, removes any doubt that the observed phenomena are LSPRs.

The numerical results also allow us to go beyond the experimental data, and to unravel the actual shape and nature of the LSPR's E-field. Figure 5 shows the resonant perpendicular electric field (Ez, along the electron beam direction) 1.5 nm into the MgO layer beneath the bottom face

of the Si_3N_4-supported Mg nanoplate. LSPR 1 is associated with two degenerate dipole resonances, a face-to-face dipole and a corner-to-corner dipole, explaining the diffuse ring pattern of the LSPR maps. LSPR 2 is associated with two close but non-degenerate modes, a (doubly degenerate) quadrupole with nodes running from four sides to the center, and a higher order mode with 6 nodes (hexapole) running from the middle of each side to the center. Both have antinodes at corners and nodes at sides, so they both produce EELS images with intensity at the corners. Finally, LSPR 3 is also associated with two close but non-degenerate modes, one with a circular node within the face of the hexagon (breathing mode[40]) and a one with a node at each corner and alternating field sign on each edge. This combination explains the unusual EELS intensity map for the third peak: the ring mode generates the intensity in the middle, while the second mode generates edge intensity with little at the corners.

Interestingly, and unlike several systems where substrate coupling leads to severe mode transformation and hybridization,[52,59,60] very similar spectral and spatial patterns are calculated for Mg NPs in vacuum, Mg/MgO NPs in vacuum, and Mg/MgO NPs on Si_3N_4 (Figure S15). A redshift is observed upon MgO coating and the addition of a substrate owing to the increase in the surrounding refractive index, but otherwise three peaks with similar ring, corner, and edge/center patterns can be observed in all cases. The electric field distribution of Mg hexagons in vacuum and Mg/MgO on Si_3N_4 is also strikingly similar (Figure S16). In fact, since the nodal structure of the six underlying modes matches very well with the first six modes for hexagonal waveguides,[61] which in turn are the first six solutions to the Helmholtz equation in a hexagon, it seems reasonable to say that these are, straightforwardly, the first six fundamental modes of any plasmonic hexagonal NPs. The modes observed also agree well with those of a Ag nanodisk mapped by Schmidt,[40,41,62] although the hexagonal geometry generates much higher field

concentration created by the sharp tips and introduces non-degenerate edge and corner hexapoles.

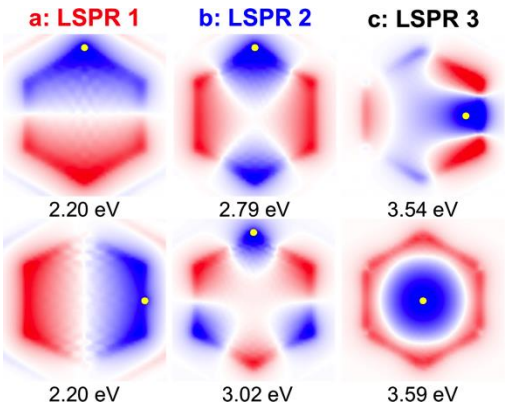

Figure 5. Calculated E-field distribution in electron-beam excited LSPRs in Mg NPs. The red and blue colors represent opposite signs of the resonant perpendicular electric field (Ez) 1.5 nm into the MgO below the bottom face of the NP, when excited by a 300 kV electron beam at the position shown as a yellow dot. a) Two degenerate modes form LSPR 1, b) two closely spaced but non-degenerate modes form LSPR 2, and c) two closely spaced but non-degenerate modes excited at different beam positions form LSPR 3.

These insights into the mode shapes allow the interpretation of the original optical spectra. The three long wavelength peaks correspond to LSPRs 1-3, as mapped with EELS. The large dipole moment of LSPR 1 couples strongly to light, so it generates the highest intensity optical peak. The constituent modes of LSPRs 2 and 3 lack dipoles, which for non-retarded cases would be optically dark. However, the current calculations and experiments use light incident at an angle, and this tilt introduces retardation across the NP face, allowing their weak optical excitation.[63] This explains the absence of these peaks in optical spectra calculated at normal incidence. The fourth optical peak corresponds to a yet higher order mode, red shifted to ~240nm by the high

index environment. Near field optical calculations confirm (Figure S8) that the first optical peaks are associated with dipole, quadruple and hexapole constituents of LSPRs 1-3 respectively. LSPR4 has a Φ shaped nodal structure and a small dipole moment, again reminiscent of modes seen in hexagonal waveguides and nanodisks.[40,61]

Concerns about the stability of Mg NPs, particularly in contrast to Ag and Au NPs, have proven unfounded. Results presented thus far were obtained on fresh (less than five weeks old) NPs. However, in the bulk, Mg forms a self-limiting oxide layer of a few nms.[44] The observed NPs are terminated by a self-limiting oxide layer as observed by STEM-EDS (Figure 1 and S3-4) and STEM-EELS (Figure S5). The stability of the Mg NPs was assessed in multiple ways, and we outline the results here, with additional results and discussion available in the Supporting Information. First, studies were performed more than three months after synthesis on NPs stored in 2-propanol in a Ar-filled glovebox, to determine the colloidal stability of the structures. Optical dark field scattering (Supplementary Video 2 and Figure S17) results were found to be indistinguishable from previous observations. SEM (Figure S18), STEM (Figure S18-19), and STEM-EELS (Figure S5, S19) studies confirm that the NP shape and the thickness of the oxide layer remain constant even after several months. Finally, STEM-EELS plasmon maps (Figure S19) further confirmed that the NPs retain their plasmonic activity after storage. Second, the stability of the NPs with respect to further oxidation, both in solution and as a dried powder, was investigated. Powder X-ray diffraction indicate our single crystalline nanoplates persist as metallic Mg for at least five and a half months when suspended in a 2-propanol solution stored in air (Figure S2). Furthermore, Mg metal persists for at least two week when the reaction product is dried to a powder and left in air (Figure S20-21), proving that the particles are at least as stable as Al NPs[10] as well as the smaller Mg NPs embedded in a polymer matrix studied by Jeon *et al.*[43]

This establishes Mg NPs as a viable plasmonic material, with stability (several months or more) comparable to Ag, Cu, and Al NPs.

In principle Mg, with its good plasmonic properties, abundance on earth, and unusual hexagonal lattice, appears to hold great promise for the burgeoning field of Earth-abundant nanoplasmonics. Here we have shown that Mg NPs deliver on the promise: they can be synthesized easily in solution, form in unusual hexagonal nanoplates (and potentially a range of exciting new shapes), sustain a range of LSPRs, and are stable in solution and when exposed to air. This work thus establishes Mg as a serious nanoplasmonic material, with great potential to be used in industrial scale applications such as photocatalysis and photodevices, where the ability to create large numbers of stable and inexpensive plasmonic NPs is critical.

METHODS

Nanoparticle Synthesis. Mg NPs were synthesized from the reduction of di-n-butylmagnesium by a lithium-naphtalene complex in tetrahydrofuran (THF) under an argon atmosphere, a procedure adapted from ref.[39] Naphtalene, Li metal, anhydrous THF, THF, 1M di-n-butylmagnesium in heptane, and 2-propanol were purchased from Sigma-Aldrich and used as received. All glassware was washed with aqua regia (1:3 HNO_3:HCl) and flame-dried under vacuum prior to use. Briefly, 2.12 g (16.2 mmol) naphthalene, 0.112 g Li (16.2 mmol), and 20 mL anhydrous THF were added to a shlenk flask under Ar atmosphere, then sonicated for 1 hour in a sealed vial. A deep green color was observed as a result of the formation of lithium naphtalide. Additional anhydrous THF (23 mL) and the Mg precursor (7 mL of 1M di-n-butylmagnesium in heptane, 7 mmol) were added under Ar atmosphere and the reaction was left

stirring overnight, with a pyrex-coated stirbar, under Ar atmosphere. The reaction was quenched by injecting ~20 mL 2-propanol, then the reaction mixture was centrifuged in a standard 50 mL plastic centrifuge tube and redispersed in THF, centrifuged again, then redispersed in 2-propanol to separate most of the the organic by-products, lithium, and naphtalene from the Mg NPs. Redispersed NPs were stored under Ar atmosphere when not in use, unless otherwise noted, and no additional surfactant or protective molecules were added.

Characterization Methods. SEM images were acquired on a FEI Helios 660 Dual Beam SEM/FIB on NPs drop cast on Si or indium tin oxide (ITO)-coated glass. All TEM, STEM, STEM-EELS, STEM-EDS, and associated data presented in the main manuscript were acquired at 300 kV on a spherical aberration corrected FEI Titan Themis^3 S/TEM equipped with a monochromator (zero loss peak full width at half maximum <0.15 eV), a Bruker Super-X quad EDS detector, and a Gatan Quantum ERS electron spectrometer. TEM and STEM analyses were performed on NPs drop cast on 10 nm Si_3N_4 membranes and rinsed with 2-propanol. Except when described otherwise, the samples were prepared under Ar atmosphere and stored in a sealed vial until they were positioned, in air, on the TEM or SEM sample holder and inserted into the instrument. The acquisition time for the ~200 pixel x 200 pixel STEM-EELS spectrum images was 0.002 s/pixel, except for the 162 nm NP, where it was 0.003 s/pixel. STEM-EDS maps were obtained by integrating the K lines of Mg, O, and Si and the L lines of Pt. Powder X-ray diffraction was performed on a Rigaku D/MAX Ultima II (Cu Kα radiation). NP tracking analysis (NTA) was performed at 405 nm (65 mW) on a Malvern NanoSight NS-300. Extinction spectra were obtained on a Varian Cary 5000 UV-Vis-NIR spectrophotometer. NPs for optical dark field measurements in 2-propanol were contained between two coverslips separated by a thin layer of 2-propanol; the coverslip edges were sealed in an Ar-filled glovebox. Dark field

optical scattering spectra were obtained on an optical microscope equipped with a halogen lamp, dark field condenser (NA: 0.85-0.95), 100X oil immersion objective (NA: 1.3), Princeton Instruments Isoplane spectrometer (50 grooves/mm) and ProEM 1024x1024 pixels EMCCD.

Numerical Methods. Optical scattering and extinction calculations were performed in the discrete dipole approximation using DDSCAT.[47,48] EELS calculations were performed using e-DDA,[54] a version of DDSCAT[47,48] modified so the incident EM field is that of a swift electron beam rather than a plane wave. All calculations were carried out with a 2 nm dipole lattice, requiring the largest calculation to include 476,270 discrete dipoles. Mg's frequency-dependent refractive index was obtained from Palik,[64] while the refractive index of vacuum, glass, 2-propanol, MgO and Si_3N_4 were fixed to 1, 1.5, 1.378, 1.7 and 2.05, respectively. In all our numerical studies, we focused on hexagonal Mg prisms, with thickness fixed to 30 nm (as observed experimentally), and tip-to-tip diameters of 162 190, 218, 246, and 272 nm. Except where otherwise stated, our calculations also include a 5 nm MgO layer around the particle, and a 20nm thick substrate beneath the NP extending at least 40 nm beyond the NP tips. Specifically, the optical calculations in Figure 2 were performed on Mg hexagonal prisms with an MgO layer, resting on a 20 nm glass substrate and otherwise in 2-propanol which were stimulated by an incident E-M beam travelling at 59 degrees to the NP's *c*-axis, with the two perpendicular polarizations averaged. The nearfield images report the Ez component of the E-Field 1.5 nm below the bottom surface of the metallic Mg in the hexagon, with excitation by the polarization of light perpendicular to the c-axis. The EELS calculations in Figure 4-5 were performed for Mg hexagonal prisms, with MgO, resting on a 20 nm Si_3N_4 substrate and otherwise in vacuum; we report the spectrum, EELS intensity images for the different peaks, and

the Ez component of the E-Field 1.5 nm below the bottom surface of the metallic Mg in the hexagon, all quantities which are direct outputs from e-DDA.

ASSOCIATED CONTENT

Supporting Information. Additional SEM images, powder X-ray diffraction pattern, nanoparticle tracking analysis results, additional composition information from EDS and EELS, NP stability study results from X-ray diffraction and optical and electron microscopy, description and full results of Gaussian fitting and other STEM-EELS analysis approaches, optical simulation results, additional EELS numerical results.

The following files are available free of charge.

Supporting figures (PDF)

Supporting videos (avi)

Conflict of Interest

The authors declare no competing financial interest.

AUTHOR INFORMATION

Corresponding Author

*Email: er407@cam.ac.uk

Author Contributions

J. S. B. performed all the numerical simulations and analyzed their results, and wrote the paper with E. R.; S. Y. acquired the transmission electron microscopy and spectroscopy data on fresh

NPs (STEM, EELS, EDS) and prepared FIB samples; E. R. designed the research, performed the synthesis and sample preparation, acquired the optical spectroscopy, X-ray diffraction, and SEM data, analyzed all the experimental data, prepared figures and wrote the paper. All authors edited the paper.

ACKNOWLEDGMENT

This research was supported by a 3M Non-Tenured Faculty award, the American Chemical Society Petroleum Research Fund (56256 DNI5) and the Binational Science Foundation. The authors wish to thank Aimé-Jean Lavigne for helpful discussions on SEM characterization, Denis Boudreau and Josée R. Daniel for assistance with the Nanosight characterization, Jiangtan Yuan and Emily Yedinak for assistance with X-ray diffraction, and Takeo Sasaki for assistance with the JEOL GRAND ARM. This research made use of instruments in the Shared Equipment Authority at Rice University.

REFERENCES

(1) Loo, C.; Lin, A.; Hirsch, L.; Lee, M.-H.; Barton, J.; Halas, N.; West, J.; Drezek, R. *Technol. Cancer Res. T.* **2004,** *3*, 33-40.
(2) Stiles, P. L.; Dieringer, J. A.; Shah, N. C.; Van Duyne, R. P. *Annu. Rev. Anal. Chem.* **2008,** *1*, 601-626.
(3) Emmanuel, F.; Samuel, G. *J. Phys. D* **2008,** *41*, 013001.
(4) Sepulveda, B.; Angelome, P. C.; Lechuga, L. M.; Liz-Marzán, L. M. *Nano Today* **2009,** *4*, 244-251.
(5) Anker, J. N.; Hall, W. P.; Lyandres, O.; Shah, N. C.; Zhao, J.; Van Duyne, R. P. *Nat. Mater.* **2008,** *7*, 442-453.
(6) Swearer, D. F.; Zhao, H.; Zhou, L.; Zhang, C.; Robatjazi, H.; Martirez, J. M. P.; Krauter, C. M.; Yazdi, S.; McClain, M. J.; Ringe, E.; Carter, E. A.; Nordlander, P.; Halas, N. J. *Proc. Natl. Acad. Sci. U.S.A.* **2016,** *113*, 8916-8920.
(7) Baffou, G.; Quidant, R. *Chem. Soc. Rev.* **2014,** *43*, 3898-3907.

(8) Chan, G. H.; Zhao, J.; Hicks, E. M.; Schatz, G. C.; Van Duyne, R. P. *Nano Lett.* **2007,** *7*, 1947-1952.
(9) Gutierrez, Y.; Ortiz, D.; Sanz, J. M.; Saiz, J. M.; Gonzalez, F.; Everitt, H. O.; Moreno, F. *Opt. Express* **2016,** *24*, 20621-20631.
(10) McClain, M. J.; Schlather, A. E.; Ringe, E.; King, N. S.; Liu, L.; Manjavacas, A.; Knight, M. W.; Kumar, I.; Whitmire, K. H.; Everitt, H. O.; Nordlander, P.; Halas, N. J. *Nano Lett.* **2015,** *15*, 2751-2755.
(11) Knight, M. W.; King, N. S.; Liu, L.; Everitt, H. O.; Nordlander, P.; Halas, N. J. *ACS Nano* **2014,** *8*, 834-840.
(12) Chan, G. H.; Zhao, J.; Schatz, G. C.; Van Duyne, R. P. *J. Phys. Chem. C* **2008,** *112*, 13958-13963.
(13) Sanz, J.; Ortiz, D.; Alcaraz De La Osa, R.; Saiz, J.; González, F.; Brown, A.; Losurdo, M.; Everitt, H.; Moreno, F. *J. Phys. Chem. C* **2013,** *117*, 19606-19615.
(14) Ekinci, Y.; Solak, H. H.; Löffler, J. F. *J. Appl. Phys.* **2008,** *104*, 083107.
(15) Meziani, M. J.; Bunker, C. E.; Lu, F.; Li, H.; Wang, W.; Guliants, E. A.; Quinn, R. A.; Sun, Y.-P. *ACS Appl. Mater. Interfaces* **2009,** *1*, 703-709.
(16) Castro-Lopez, M.; Brinks, D.; Sapienza, R.; van Hulst, N. F. *Nano Lett.* **2011,** *11*, 4674-4678.
(17) Maidecchi, G.; Gonella, G.; Proietti Zaccaria, R.; Moroni, R.; Anghinolfi, L.; Giglia, A.; Nannarone, S.; Mattera, L.; Dai, H.-L.; Canepa, M.; Bisio, F. *ACS Nano* **2013,** *7*, 5834-5841.
(18) Zhou, L.; Zhang, C.; McClain, M. J.; Manjavacas, A.; Krauter, C. M.; Tian, S.; Berg, F.; Everitt, H. O.; Carter, E. A.; Nordlander, P.; Halas, N. J. *Nano Lett.* **2016,** *16*, 1478-1484.
(19) Blaber, M. G.; Arnold, M. D.; Ford, M. J. *J. Phys.: Condens. Matter* **2010,** *22*, 143201.
(20) McMahon, J. M.; Schatz, G. C.; Gray, S. K. *Phys. Chem. Chem. Phys.* **2013,** *15*, 5415-5423.
(21) Sanz, J. M.; Ortiz, D.; Alcaraz de la Osa, R.; Saiz, J. M.; González, F.; Brown, A. S.; Losurdo, M.; Everitt, H. O.; Moreno, F. *J. Phys. Chem. C* **2013,** *117*, 19606-19615.
(22) Yang, Y.; Callahan, J. M.; Kim, T.-H.; Brown, A. S.; Everitt, H. O. *Nano Lett.* **2013,** *13*, 2837-2841.
(23) Knight, M. W.; Coenen, T.; Yang, Y.; Brenny, B. J. M.; Losurdo, M.; Brown, A. S.; Everitt, H. O.; Polman, A. *ACS Nano* **2015,** *9*, 2049-2060.
(24) Alcaraz de la Osa, R.; Sanz, J. M.; Barreda, A. I.; Saiz, J. M.; González, F.; Everitt, H. O.; Moreno, F. *J. Phys. Chem. C* **2015,** *119*, 12572-12580.
(25) Watson, A. M.; Zhang, X.; Alcaraz de la Osa, R.; Sanz, J. M.; González, F.; Moreno, F.; Finkelstein, G.; Liu, J.; Everitt, H. O. *Nano Lett.* **2015,** *15*, 1095-1100.
(26) Guler, U.; Boltasseva, A.; Shalaev, V. M. *Science* **2014,** *344*, 263.
(27) Guler, U.; Shalaev, V. M.; Boltasseva, A. *Mater. Today* **2015,** *18*, 227-237.
(28) Khurgin, J. B. *Philos. Trans. Royal Soc. A* **2017,** *375*.
(29) Murray, W. A.; Barnes, W. L. *Adv. Mater.* **2007,** *19*, 3771-3782.
(30) Dionne, J. A.; Atwater, H. A. *MRS Bull.* **2012,** *37*, 717-724.
(31) West, P. R.; Ishii, S.; Naik, G. V.; Emani, N. K.; Shalaev, V. M.; Boltasseva, A. *Laser Photonics Rev.* **2010,** *4*, 795-808.
(32) Naik Gururaj, V.; Shalaev Vladimir, M.; Boltasseva, A. *Adv. Mater.* **2013,** *25*, 3264-3294.
(33) Sharma, B.; Frontiera, R. R.; Henry, A.-I.; Ringe, E.; Van Duyne, R. P. *Mater. Today* **2012,** *15*, 16-25.
(34) Boltasseva, A.; Atwater, H. A. *Science* **2011,** *331*, 290.
(35) Jeong, H.-H.; Mark, A. G.; Fischer, P. *Chem. Comm.* **2016,** *52*, 12179-12182.

(36) Sterl, F.; Strohfeldt, N.; Walter, R.; Griessen, R.; Tittl, A.; Giessen, H. *Nano Lett.* **2015,** *15*, 7949-7955.
(37) Wang, Y.; Peterson, E. M.; Harris, J. M.; Appusamy, K.; Guruswamy, S.; Blair, S. *J. Phys. Chem. C* **2017,** *121*, 11650-11657.
(38) Duan, X.; Kamin, S.; Liu, N. *Nat. Comm.* **2017,** *8*, 14606.
(39) Liu, W.; Aguey, Z.; Kondo, F. *J. Mater. Chem. A* **2014,** *2*, 9718-9726.
(40) Schmidt, F.-P.; Ditlbacher, H.; Hohenester, U.; Hohenau, A.; Hofer, F.; Krenn, J. R. *Nano Lett.* **2012,** *12*, 5780-5783.
(41) Schmidt, F.-P.; Ditlbacher, H.; Hohenester, U.; Hohenau, A.; Hofer, F.; Krenn, J. R. *Nat. Comm.* **2014,** *5*, 3604.
(42) Moon, H. R.; Urban, J. J.; Milliron, D. J. *Angew. Chem. Int. Ed.* **2009,** *48*, 6278-6281.
(43) Jeon, K.-J.; Moon, H. R.; Ruminski, A. M.; Jiang, B.; Kisielowski, C.; Bardhan, R.; Urban, J. J. *Nat. Mater.* **2011,** *10*, 286.
(44) Feliu Jr, S.; Galván, J.; Pardo, A.; Merino, M.; Arrabal, R. *Open Corros. J.* **2010,** *3*, 80-90.
(45) Ringe, E.; Sharma, B.; Henry, A.-I.; Marks, L. D.; Van Duyne, R. P. *Phys. Chem. Chem. Phys.* **2013,** *15*, 4110-4129.
(46) Ringe, E.; Langille, M. R.; Sohn, K.; Zhang, J.; Huang, J.; Mirkin, C. A.; Van Duyne, R. P.; Marks, L. D. *J. Phys. Chem. Lett.* **2012,** *3*, 1479-1483.
(47) Draine, B. T.; Flatau, P. J. *J. Opt. Soc. Am. A* **1994,** *11*, 1491-1499.
(48) Flatau, P. J.; Draine, B. T. *Opt. Express* **2014,** *22*, 21834-21846.
(49) Schaffer, B.; Hohenester, U.; Trügler, A.; Hofer, F. *Phys. Rev. B* **2009,** *79*, 041401.
(50) Collins, S. M.; Ringe, E.; Duchamp, M.; Saghi, Z.; Dunin-Borkowski, R. E.; Midgley, P. A. *ACS Photon.* **2015,** *2*, 1628-1635.
(51) Yazdi, S.; Daniel, J. R.; Large, N.; Schatz, G. C.; Boudreau, D.; Ringe, E. *Nano Lett.* **2016,** *16*, 6939-6945.
(52) Kadkhodazadeh, S.; Christensen, T.; Beleggia, M.; Mortensen, N. A.; Wagner, J. B. *ACS Photon.* **2017,** *4*, 251-261.
(53) Nicoletti, O.; de la Peña, F.; Leary, R. K.; Holland, D. J.; Ducati, C.; Midgley, P. A. *Nature* **2013,** *502*, 80.
(54) Bigelow, N. W.; Vaschillo, A.; Iberi, V.; Camden, J. P.; Masiello, D. J. *ACS Nano* **2012,** *6*, 7497-7504.
(55) Nelayah, J.; Kociak, M.; Stephan, O.; de Abajo, F.; Tence, M.; Henrard, L.; Taverna, D.; Pastoriza-Santos, I.; Liz-Marzan, L.; Colliex, C. *Nat. Phys.* **2007,** *3*, 348 - 353.
(56) Colliex, C.; Kociak, M.; Stéphan, O. *Ultramicroscopy* **2016,** *162*, A1-A24.
(57) Ringe, E.; DeSantis, C. J.; Collins, S. M.; Duchamp, M.; Dunin-Borkowski, R. E.; Skrabalak, S. E.; Midgley, P. A. *Sci. Rep.* **2015,** *5*, 17431.
(58) Kelly, K. L.; Coronado, E.; Zhao, L. L.; Schatz, G. C. *J. Phys. Chem. B* **2003,** *107*, 668-677.
(59) Cherqui, C.; Li, G.; Busche, J. A.; Quillin, S. C.; Camden, J. P.; Masiello, D. J. *J. Phys. Chem. Lett.* **2018**.
(60) Cherqui, C.; Li, G.; Busche, J. A.; Quillin, S. C.; Camden, J. P.; Masiello, D. J. *J. Phys. Chem. Lett.* **2018,** *9*, 504-512.
(61) Bauer, L.; Reiss, E. L. *SIAM J. Appl. Math.* **1978,** *35*, 508-514.
(62) Schmidt, F. P.; Ditlbacher, H.; Hofer, F.; Krenn, J. R.; Hohenester, U. *Nano Lett.* **2014,** *14*, 4810-4815.
(63) Hao, F.; Larsson, E. M.; Ali, T. A.; Sutherland, D. S.; Nordlander, P. *Chem. Phys. Lett.* **2008,** *458*, 262-266.

(64) Palik, E. D., *Handbook of optical constants of solids*. Academic press: Cambridge, MA, 1998; Vol. 3.

TOC GRAPHIC